Journal of Advanced Ceramics
2022, **11**(10): 1654–1670
https://doi.org/10.1007/s40145-022-0638-7

ISSN 2226-4108
CN 10-1154/TQ

Research Article

New class of high-entropy pseudobrookite titanate with excellent thermal stability, low thermal expansion coefficient, and low thermal conductivity

Jinyu WU, Xiaohui MA, Xiaoxia HU, Liwen YAN, Feng HOU, Jiachen LIU, Anran GUO*

School of Materials Science and Engineering, *Key Laboratory of Advanced Ceramics and Machining Technology of Ministry of Education*, *Tianjin University*, *Tianjin 300072*, *China*

Received: May 31, 2022; Revised: July 31, 2022; Accepted: August 9, 2022

Abstract: As a type of titanate, the pseudobrookite (MTi_2O_5/M_2TiO_5) exhibits a low thermal expansion coefficient and thermal conductivity, as well as excellent dielectric and solar spectrum absorption properties. However, the pseudobrookite is unstable and prone to decomposing below 1200 ℃, which limits the practical application of the pseudobrookite. In this paper, the high-entropy pseudobrookite ceramic is synthesized for the first time. The pure high-entropy $(Mg,Co,Ni,Zn)Ti_2O_5$ with the pseudobrookite structure and the biphasic high-entropy ceramic composed of the high-entropy pseudobrookite $(Cr,Mn,Fe,Al,Ga)_2TiO_5$ and the high-entropy spinel $(Cr,Mn,Fe,Al,Ga,Ti)_3O_4$ are successfully prepared by the *in-situ* solid-phase reaction method. The comparison between the theoretical crystal structure of the pseudobrookite and the aberration-corrected scanning transmission electron microscopy (AC-STEM) images of high-entropy $(Mg,Co,Ni,Zn)Ti_2O_5$ shows that the metal ions (M and Ti ions) are disorderly distributed at the A site and the B site in high-entropy $(Mg,Co,Ni,Zn)Ti_2O_5$, leading to an unprecedentedly high configurational entropy of high-entropy $(Mg,Co,Ni,Zn)Ti_2O_5$. The bulk high-entropy $(Mg,Co,Ni,Zn)Ti_2O_5$ ceramics exhibit a low thermal expansion coefficient of 6.35×10^{-6} K^{-1} in the temperature range of 25–1400 ℃ and thermal conductivity of 1.840 $W\cdot m^{-1}\cdot K^{-1}$ at room temperature, as well as the excellent thermal stability at 200, 600, and 1400 ℃. Owing to these outstanding properties, high-entropy $(Mg,Co,Ni,Zn)Ti_2O_5$ is expected to be the promising candidate for high-temperature thermal insulation. This work has further extended the family of different crystal structures of high-entropy ceramics reported to date.

Keywords: high-entropy pseudobrookite; $(Mg,Co,Ni,Zn)Ti_2O_5$; $(Cr,Mn,Fe,Al,Ga)_2TiO_5$; high conformational entropy; thermal expansion coefficient; thermal conductivity

* Corresponding author.
E-mail: arguo@tju.edu.cn

1 Introduction

The concept of high-entropy materials is proposed in the field of alloys firstly. Compared with the traditional alloys, high-entropy alloys take a variety of elements as the principal elements in approximately equal proportions. Multi-principal elements increase the configurational entropy and reduce the Gibbs free energy for the formation of multiphase solid solutions. Therefore, high-entropy alloys exhibit excellent structural stability and physical properties [1,2]. Subsequently, the concept of high-entropy materials and the four major effects (high configurational entropy, severe lattice distortion, sluggish diffusion, and "cocktail" effect) are further extended to the field of ceramics [3–5]. High-entropy ceramics with various excellent properties have been developed successively [6–11], and the compositionally complex ceramics (CCCs) with more flexible principal element numbers and content range are further proposed [12,13]. Research on high-entropy ceramics has included a variety of crystal structures such as rock salt structure, pyrochlore structure, perovskite structure, argyrodite structure, fluorite structure, spinel structure, hexagonal $CrSi_2$-type structure, hexagonal AlB_2-type structure, aluminates, silicates, and borides [3–18]. However, to the best of our knowledge, there is no research on the fabrication of the high-entropy ceramics with the pseudobrookite structure.

Most of the pseudobrookite belong to titanate (MTi_2O_5/M_2TiO_5), orthorhombic system, and are in the *Cmcm* space group. Their crystal structure is composed of two kinds of strongly distorted octahedra [AO_6] and [BO_6] (Wyckoff positions 4c and 8f), in which A and B sites are occupied by the metal ions M and Ti, respectively. The [MO_6] and [TiO_6] are connected in the form of common edge along the directions of *b* and *c* axes, and connected in a co-top manner along the direction of *a* axis. The lattice parameters in the directions of *b* and *c* axes are much higher than that in the direction of *a* axis. At the same time, the A site and the B site in the pseudobrookite phase have extraordinary structure flexibility, in which the M and Ti disorderly distributed in different degrees. So the general formula can also be written as $[M^{3+},M^{2+},Ti]^A[Ti,M^{2+},M^{3+}]^B{}_2O_5$ [19–21].

Owing to the special crystal structure of pseudobrookite, the thermal expansion coefficient of single crystal in the *a*-axis direction is significantly lower than that in the other two axes. Due to the anisotropic thermal expansion coefficient of the single crystal, a large number of microcracks are formed in the pseudobrookite ceramics during the sintering process. The microcracks can provide space for thermal expansion and effectively relieve stress concentrations, resulting in a particularly small thermal expansion coefficient and excellent thermal shock resistance of the pseudobrookite ceramics at the macroscopic scale [22,23]. For $MgTi_2O_5$, the presence of microcracks effectively reduces the linear thermal expansion from 9.5% to 5.2%, from room temperature (RT) to 1000 ℃ [23]. For Al_2TiO_5, it exhibits a low thermal expansion coefficient of 2.5×10^{-6} K^{-1} in the temperature range of 25–1400 ℃ due to the presence of microcracks [24]. Moreover, the pseudobrookite also exhibits a low thermal conductivity and a high melting point. Therefore, the pseudobrookite has been widely used as high-temperature insulation ceramics [24], water purification filters [25], and diesel particulate filters [23]. On the other hand, as an n-type semiconductor, the pseudobrookite exhibits excellent dielectric and impedance properties as well as suitable electronic structure, band gap, and solar spectral absorption properties, which can be used as photocatalytic materials [26–30], thermoelectric materials [31], gas sensors [32], humidity sensors [33], microwave absorbing materials [34], anode materials of solid oxide fuel cells [35], and ceramic pigments [36–40].

However, the pseudobrookite is unstable and prone to decomposing below 1200 ℃, which seriously limits its further application. For instance, the Al_2TiO_5 phase decomposes into Al_2O_3 and TiO_2 at 750–1280 ℃ [24,40,41], the $MgTi_2O_5$ phase decomposes at 130–230 or below 620 ℃ [23,42], and the Ga_2TiO_5 phase can only exist at high temperatures [43]. This is attributed to the fact that the pseudobrookite is an infrequent phase stabilized by entropy. Unlike ordinary compounds that obtain a lower Gibbs free energy by lower formation enthalpy, the pseudobrookite has a high configurational entropy, which allows the pseudobrookite to obtain a low Gibbs free energy at high temperatures. However, the Gibbs free energy is not low enough to keep the pseudobrookite stable below 1200 ℃. Therefore, the method of introducing transition metal elements to form solid solutions is widely used to prevent the decomposition and improve the mechanical property of pseudobrookite [24,31,34,36–38,41]. However, the solubility limit of a single doped phase prevents further development [38–40,44].

Herein, we successfully prepare high-entropy

pseudobrookite for the first time to further increase the configurational entropy and improve the thermal stability of the pseudobrookite. Two kinds of typical pseudobrookite systems, $A(M^{2+})Ti_2O_5$ and $B(M^{3+})_2TiO_5$, are selected. Mg, Co, Ni, and Zn are selected for the M position in ATi_2O_5 (AT2), and Al, Ga, Fe, Cr, and Mn are selected for the M position in B_2TiO_5 (B2T). The high-entropy pseudobrookite $(Mg,Co,Ni,Zn)Ti_2O_5$ and $(Al,Ga,Fe,Cr,Mn)_2TiO_5$ are synthesized by the traditional *in-situ* solid-phase reaction method. The formation process of the high-entropy pseudobrookite is determined from the aspects of crystal structure, chemical composition, microstructure, chemical states, and chemical environment of metal ions. The results show that high-entropy $(Mg,Co,Ni,Zn)Ti_2O_5$ has a high configurational entropy and excellent thermal stability. The dense high-entropy $(Mg,Co,Ni,Zn)Ti_2O_5$ also exhibits a low thermal expansion coefficient and a low thermal conductivity.

2 Experimental

2. 1 Preparation

The high-entropy pseudobrookite AT2 and B2T were prepared by the *in-situ* solid-phase reaction method. MgO (99.9% purity), ZnO (99.99% purity), Al_2O_3 (99.99% purity), Ga_2O_3 (99.99% purity), Fe_2O_3 (99.9% purity), and Cr_2O_3 (99.95% purity) (Macklin Biochemical Co., Ltd., Shanghai, China) and CoO (99.0% purity), NiO (99.0% purity), MnO (99.5% purity), and TiO_2 (rutile, 99.8% purity) (Aladdin Biochemical Technology Co., Ltd., Shanghai, China) were used as the raw powders. Firstly, the raw powders were weighed according to the stoichiometric ratio, and were ball-milled at 200 r/min for 7 h with ethanol as the dispersing phase. The slurry after ball milling was thoroughly dried in an oven at 60 ℃ to remove ethanol, and then sieved by the 60-mesh sieve to obtain the mixed raw material powders. Polyvinyl alcohol (PVA) was added into the mixed raw material powders as the binder, and the mixed raw material powders were pressed into columnar-shaped compacts with a diameter of 20 mm under a uniaxial pressure of 30 MPa. Finally, the green bodies were sintered at different temperatures (1100, 1200, 1300, and 1400 ℃) for 2 h in the air.

2. 2 Characterizations

The crystal structures of the specimens were analyzed via the X-ray diffractometer (Rigaku, D/Max-2500, Japan) ranging from 10° to 90° with filtered Cu Kα radiation. The scanning electron microscope (Hitachi, S-4800, Japan) and the energy disperse spectrometer (Oxford, X-Max20, UK) were used to characterize the microstructures and the element distributions of the specimens, respectively. The quantitative analysis of the composition was realized by the energy disperse spectrometer (Oxford, X-Max20, UK), inductively the coupled plasma-optical emission spectrometer (Agilent, 5110, USA), and the X-ray fluorescence spectrometer (Rigaku, Supermini200, Japan). The chemical states and chemical environment of the metal elements in the high-entropy MTi_2O_5 were analyzed by the X-ray photoelectron spectrometer (Kratos, Axis supra, UK) with Al Kα X-ray source and pass energy of 40 eV. All data were calibrated to the adventitious C 1s peak at 284.8 eV. The high-resolution microstructure and crystal structure of the high-entropy MTi_2O_5 were studied by the transmission electron microscope (JEOL, Jem-2100f, Japan) and the aberration-corrected scanning transmission electron microscope (JEOL, Jem-arm200f, Japan). The thermal expansion coefficients of the high-entropy MTi_2O_5 were measured by the thermal dilatometer (Netzsch, Dil402 expedis supreme, Germany) under the protection of argon flow. The thermal conductivity of $MgTi_2O_5$, $CoTi_2O_5$, and the high-entropy MTi_2O_5 were obtained by the transient plane source (TPS) method (Hot Disk, Tps2500s, Sweden). The bulk density of the samples was tested by the Archimede's method.

3 Results and discussion

The pseudobrookite is an infrequent phase stabilized by entropy. The A site and B site in the pseudobrookite have extraordinary structure flexibility, in which the M and Ti disorderly distribute in some degrees. This disordered distribution provides a relatively high configurational entropy for the pseudobrookite, which makes the pseudobrookite have a low Gibbs free energy at high temperatures. However, the degree of disorder distribution is limited at lower temperatures, resulting in the instability and decomposition of pseudobrookite. As a comparison, the degree of disordered distribution improves considerably in high-entropy pseudobrookite at the same temperature. The ideal crystal structure of high-entropy pseudobrookite is shown in Fig. 1, in which the metal ions M and Ti are

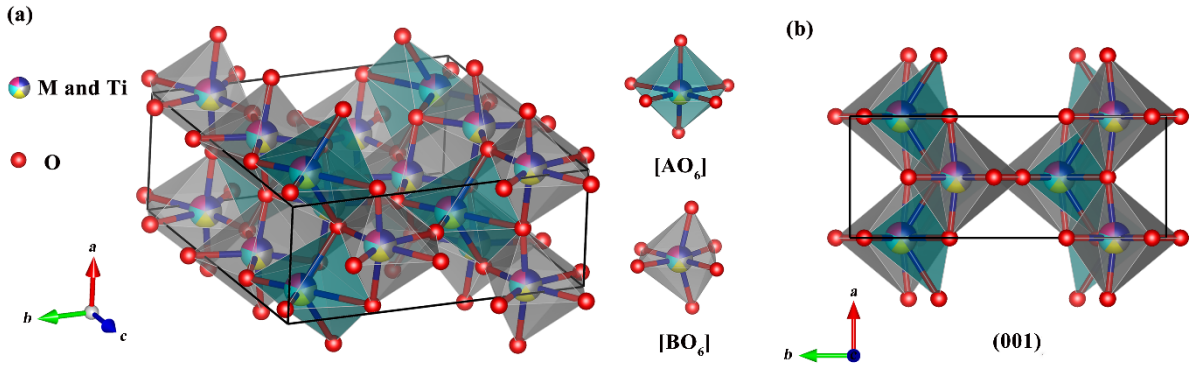

Fig. 1 (a) Ideal crystal structure with the most disordered state of the high-entropy pseudobrookite phase; (b) the (001) crystal plane of the ideal crystal structure of the high-entropy pseudobrookite phase.

randomly distributed at the A site and the B site. In this work, Mg, Co, Ni, and Zn were selected for the M position in AT2 system, and Al, Ga, Fe, Cr, and Mn were selected for the M position in B2T system. These metal elements have been proved to have good compatibility and high doping amounts in the lattice of pseudobrookite [32,34,35,37,38,43].

3. 1 Synthesis and characterization of high-entropy (Mg,Co,Ni,Zn)Ti_2O_5

The X-ray diffraction (XRD) patterns of AT2 after sintering at 1100, 1200, 1300, and 1400 ℃ are shown in Fig. 2. It can be seen that the main phases of AT2 after sintering at 1100 ℃ are the ilmenite phase high-entropy (Mg,Co,Ni,Zn)TiO_3 (space group *R*3) and rutile phase TiO_2, which are consistent with the stoichiometric ratio of the original raw material. When

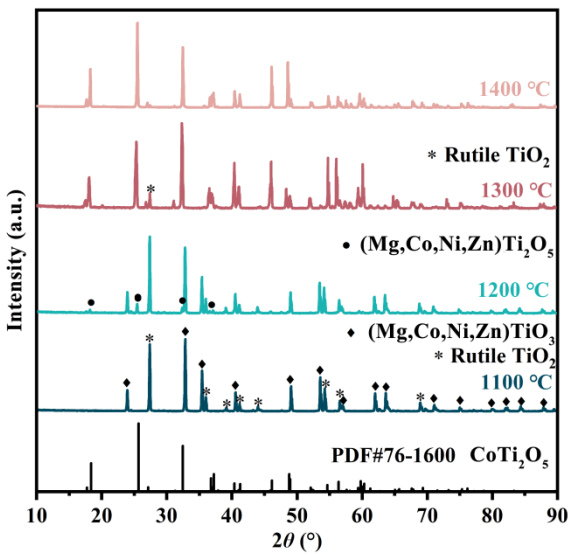

Fig. 2 XRD patterns of AT2 after sintering at 1100, 1200, 1300, and 1400 ℃ for 2 h.

the sintering temperature is increased to 1200 ℃, a small amount of pseudobrookite phase begins to appear. With a further increase in the sintering temperature, the ilmenite phase high-entropy (Mg,Co,Ni,Zn)TiO_3 gradually reacts with TiO_2 to form the pseudobrookite phase high-entropy (Mg,Co,Ni,Zn)Ti_2O_5. As the sintering temperature is further increased to 1400 ℃, the XRD spectra are indexed to the pure pseudobrookite phase high-entropy (Mg,Co,Ni,Zn)Ti_2O_5. Therefore, we can conclude that raw material powders (MgO, CoO, NiO, ZnO, and TiO_2) are firstly reacted with each other to form high-entropy (Mg,Co,Ni,Zn)TiO_3 phase, and then high-entropy (Mg,Co,Ni,Zn)TiO_3 further reacts with TiO_2 to form high-entropy (Mg,Co,Ni,Zn)Ti_2O_5. Similar process has also been found in the synthesis of other pseudobrookite phase. In the study of preparing single crystal $CoTi_2O_5$ [45], it was found that CoO first reacted with TiO_2 to form $CoTiO_3$, and then the single crystal $CoTi_2O_5$ formed along the interface between $CoTiO_3$ and TiO_2. And the same process has also been found in the preparation of $MgTi_2O_5$ by different methods [23,25,37,46].

To demonstrate the existence of the transition phase high-entropy (Mg,Co,Ni,Zn)TiO_3, the phase compositions of AT2 after sintering at 1100 ℃ were further investigated. Figure 3 shows the SEM image and the corresponding energy dispersive spectroscopy (EDS) mappings of the bulk AT2 after sintering at 1100 ℃. In Fig. 3, Mg, Co, Ni, and Zn show a significant aggregation, and the quantitative analysis results of the Mg, Co, Ni, Zn, and Ti in these aggregated areas are consistent with the components of high-entropy (Mg,Co,Ni,Zn)TiO_3. This result confirms the existence of the transition phase high-entropy (Mg,Co,Ni,Zn)TiO_3.

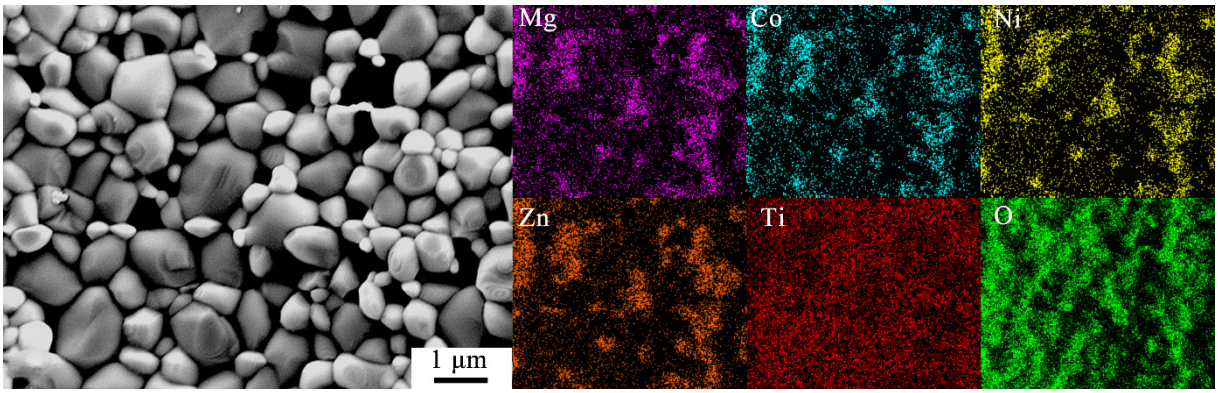

Fig. 3 SEM image and corresponding EDS mappings of AT2 after sintering at 1100 ℃.

The SEM images and corresponding EDS mappings of pure pseudobrookite phase high-entropy $(Mg,Co,Ni,Zn)Ti_2O_5$ after sintering at 1400 ℃ are shown in Fig. 4. As shown in Fig. 4(a), high-entropy $(Mg,Co,Ni,Zn)Ti_2O_5$ is mainly composed of some abnormally large rod-shaped particles and equiaxed fine particles around the rod-shaped particles. The corresponding EDS mappings show that the Mg, Co, Ni, Zn, Ti, and O are evenly distributed without obvious element enrichment. Figures 4(b) and 4(c) show the SEM images and corresponding EDS mappings of the abnormally large rod-shaped particles and the fine particles, respectively. All elements in the rod-shaped particles and the equiaxed particles are distributed homogeneously. Combined with the XRD analysis results, it can be concluded that the rod-shaped particles and the equiaxed fine particles all belong to high-entropy $(Mg,Co,Ni,Zn)Ti_2O_5$. The morphology of the coexistence of the rod-shaped particles and the equiaxed fine particles is consistent with that of the normal pseudobrookite phase [23–25,31,32,41,47]. The appearance of the rod-shaped particles is attributed to the exaggerated grain growth (EGG) of some particles at high temperatures [48]. For the pseudobrookite phase, the lattice parameters in the directions of *b* and *c* axes are much higher than that in the direction of *a* axis, indicating that the reticular density of the (100) crystal plane is less than that of the (010) and (001) crystal planes. According to the Bravais' rule, the crystals are usually surrounded by crystallographic planes with the highest reticular densities and the greatest interplanar distances. Therefore, the (010) and (001) crystal planes extend along the *a*-axis direction continuously during the crystal growth at high temperatures, which eventually leads to some of the crystals showing a rod-shaped structure.

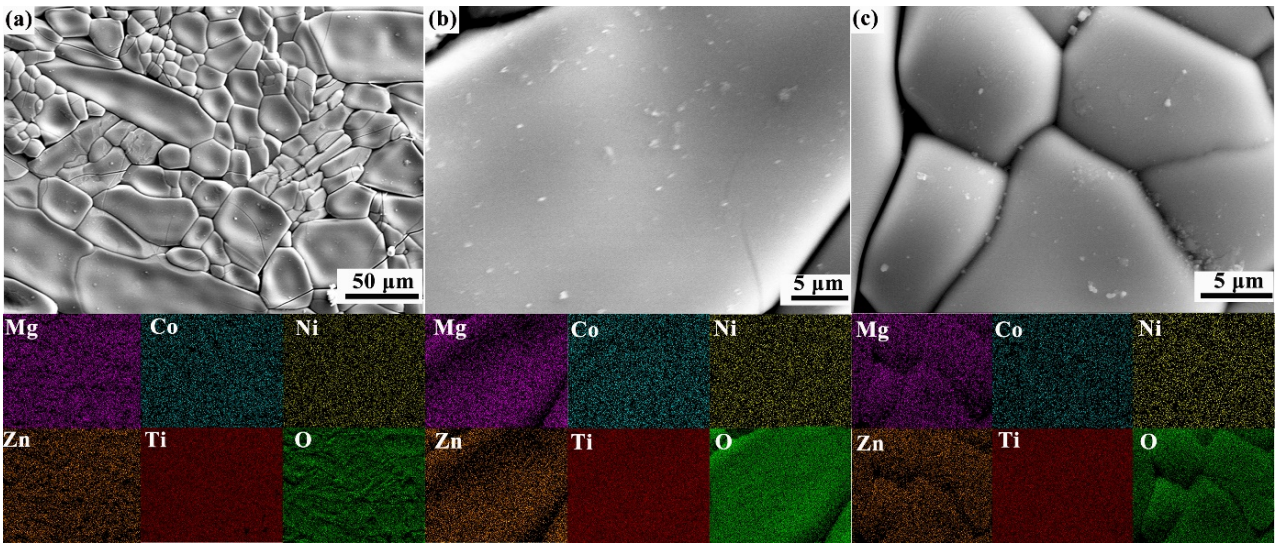

Fig. 4 (a) SEM image and corresponding EDS mappings of AT2; SEM images and corresponding EDS mappings of (b) abnormally large rod-shaped particles and (c) fine particles in AT2 after sintering at 1400 ℃.

In order to determine the element compositions of high-entropy (Mg,Co,Ni,Zn)Ti_2O_5, quantitative analysis of each element was carried out by three different methods (EDS, XRF, and ICP). The corresponding results are listed in Table 1. Firstly, the ratio of metal ions M (Mg, Co, Ni, and Zn) to Ti is in accord with the stoichiometric ratio of MTi_2O_5 (1:2). Furthermore, all the analyses show that the contents of Mg, Co, and Ni ions are in line with the expected content of high-entropy $(Mg_{0.25}Co_{0.25}Ni_{0.25}Zn_{0.25})Ti_2O_5$, and the content of Zn ions is slightly lower than the expected content (0.25). The slightly lower concentration of Zn ions is caused by the lower capacity of Zn in the pseudobrookite phase [27,35] and the volatilization of ZnO/Zn [35]. In addition, the rod-shaped particles have the same element composition as the equiaxed particles. All the results demonstrate that AT2 is consisted of pure pseudobrookite phase high-entropy (Mg,Co,Ni,Zn)Ti_2O_5 after sintering at 1400 ℃. We have successfully prepared pure high-entropy pseudobrookite ceramics for the first time.

3. 2 Synthesis and characterization of high-entropy $(Cr,Mn,Fe,Al,Ga)_2TiO_5$

The XRD patterns of B2T after sintering at different temperatures are shown in Fig. 5. The main crystalline phase in B2T after sintering at 1100 ℃ is the cubic spinel phase high-entropy $(Cr,Mn,Fe,Al,Ga,Ti)_3O_4$ with the $Fm\bar{3}m$ space group. As the sintering temperature is increased to above 1200 ℃, the pseudobrookite phase high-entropy $(Cr,Mn,Fe,Al,Ga)_2TiO_5$ begins to appear. When the sintering temperature is 1400 ℃, B2T is composed of the pseudobrookite phase high-entropy $(Cr,Mn,Fe,Al,Ga)_2TiO_5$ and the spinel phase high-entropy $(Cr,Mn,Fe,Al,Ga,Ti)_3O_4$. It can be seen that the formation process of high-entropy (Cr,Mn,Fe,Al,Ga)$_2TiO_5$ in B2T does not have any transition phase. This similar process has also been reported in related studies. For example, Fe_2TiO_5 was also found to be directly formed by the diffusion of Ti^{4+} to the surface of Fe_2O_3 [32], and Al_2O_3 reacted directly with TiO_2 to form Al_2TiO_5 [40].

Table 1 Quantitative analysis of AT2 after sintering at 1400 ℃ (relative ratios of the molar content of each element)

	Mg	Co	Ni	Zn	Ti
EDS (rod-shaped particles)	0.258	0.273	0.275	0.194	2.057
EDS (equiaxed particles)	0.259	0.262	0.262	0.217	1.976
EDS (whole AT2)	0.255	0.266	0.265	0.224	2.005
XRF	0.310	0.234	0.252	0.204	1.949
ICP	0.262	0.244	0.266	0.228	1.986

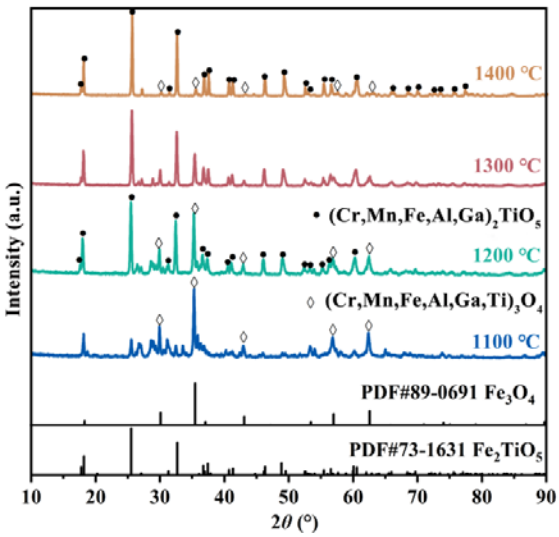

Fig. 5 XRD patterns of B2T after sintering at 1100, 1200, 1300, and 1400 ℃ for 2 h.

As shown in Fig. 6, the surface morphology images of the bulk B2T after sintering at 1400 ℃ are mainly composed of a large number of equiaxed particles. In contrast to the AT2 (pure pseudotitanite phase) where some particles undergo the EGG to form the rod-shaped structure, the high-entropy spinel phase (Cr,Mn,Fe,Al,Ga,Ti)$_3O_4$ generated firstly in B2T prevents further growth of the high-entropy pseudobrookite phase $(Cr,Mn,Fe,Al,Ga)_2TiO_5$, resulting in the formation of equiaxed grains. Figure 6 also shows the corresponding EDS mappings, in which Cr, Mn, Fe, Al, Ga, and Ti elements are distributed homogeneously. The quantitative results obtained by the XRF, ICP, and EDS test are listed in Table 2. The EDS results exhibit two kinds of different element distribution trends, which conformed to the chemical compositions of the pseudobrookite phase high-entropy $(Cr,Mn,Fe,Al,Ga)_2TiO_5$ and the spinel phase high-entropy $(Cr,Mn,Fe,Al,Ga,Ti)_3O_4$. It can indicate that B2T after sintering at 1400 ℃ is a biphasic high-entropy ceramic composed of the high-entropy pseudobrookite $(Cr,Mn,Fe,Al,Ga)_2TiO_5$ and the high-entropy spinel $(Cr,Mn,Fe,Al,Ga,Ti)_3O_4$. In high-entropy $(Cr,Mn,Fe,Al,Ga)_2TiO_5$, the Cr and Mn have a lower content, while Fe has a higher content. Contrary to the EDS results of high-entropy $(Cr,Mn,Fe,Al,Ga)_2TiO_5$, the contents of Cr and Mn in high-entropy $(Cr,Mn,Fe,Al,Ga,Ti)_3O_4$ are significantly

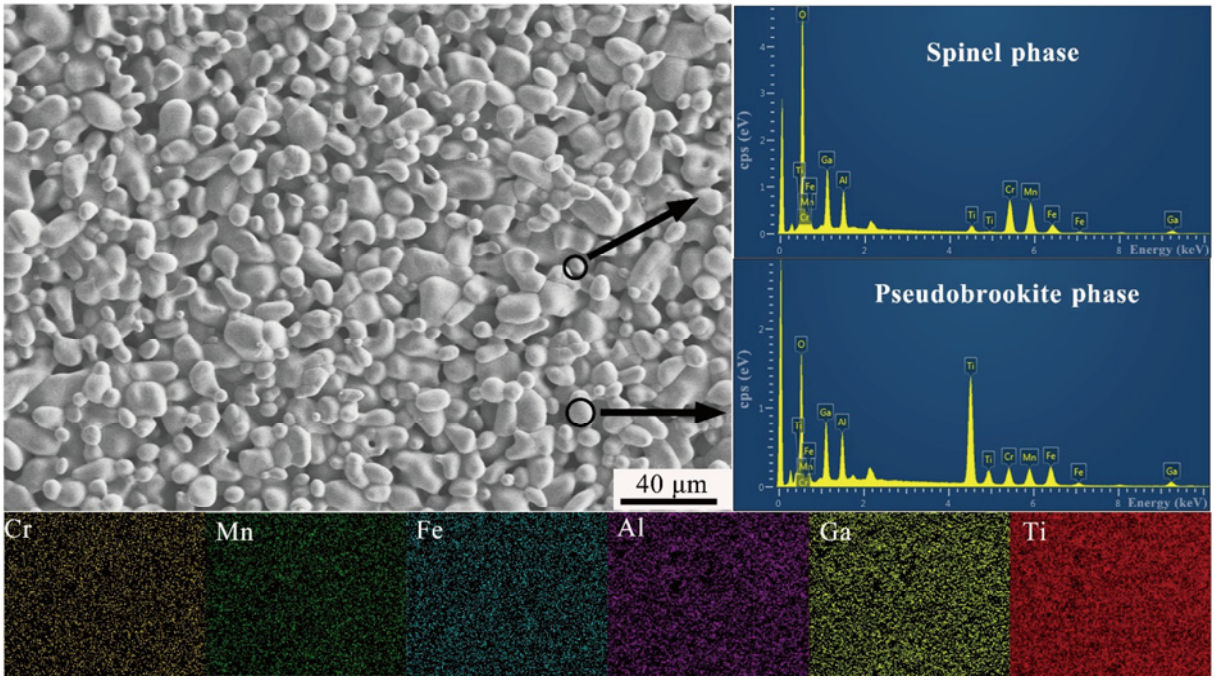

Fig. 6 Surface morphology image and corresponding EDS mappings of B2T after sintering at 1400 ℃.

Table 2 Quantitative analysis of B2T after sintering at 1400 ℃ (relative ratios of the molar content of each element)

	Cr	Mn	Fe	Al	Ga	Ti
XRF	0.193	0.200	0.196	0.213	0.198	0.504
ICP	0.156	0.174	0.247	0.199	0.224	0.637
EDS (pseudobrookite)	0.149	0.164	0.241	0.219	0.227	0.698
EDS (spinel)	0.262	0.262	0.086	0.172	0.218	0.048

higher than those of the other metal elements M, while the content of Fe is far lower than those of the other metal elements M. The reason for the opposite distribution trends of Cr, Mn, and Fe in the pseudobrookite phase high-entropy $(Cr,Mn,Fe,Al,Ga)_2TiO_5$ and the spinel phase high-entropy $(Cr,Mn,Fe,Al,Ga,Ti)_3O_4$ is that Cr and Mn tend to enter the spinel phase, while Fe tends to enter the inverse spinel phase. During the formation of the spinel phase, the total free energy of the spinel phase is the lowest when Cr, Al, and Ga ions occupy the octahedral positions, and Mn ions occupy the tetrahedral positions [49–54]. In contrast, Fe tends to form the inverse spinel structure and occupies the tetrahedral position in the inverse spinel structure [50,53]. Therefore, during the formation of the high-entropy spinel $(Cr,Mn,Fe,Al,Ga,Ti)_3O_4$, more Cr and Mn ions enter the lattice of the spinel, while only a very small amount of Fe ion enters the lattice of the spinel. With the further increase of temperature, the remaining oxides react with each other to form the high-entropy pseudobrookite $(Cr,Mn,Fe,Al,Ga)_2TiO_5$.

The XRF test can show the overall content of B2T in the macro perspective, and the results exhibit that the content of each element in B2T after sintering at 1400 ℃ is consistent with that of the raw material, indicating no element volatilization during the sintering process. The results of the ICP are almost the same as those of high-entropy $(Cr,Mn,Fe,Al,Ga)_2TiO_5$ in the EDS. We consider that the dissolution solution used in the chemical dissolution process was more favorable to dissolve the pseudobrookite phase (the same dissolution solution was also used in the ICP test of AT2). Thus, during the ICP test, more high-entropy pseudobrookite phase was dissolved than the high-entropy spinel phase.

The synthesis process of high-entropy $(Mg,Co,Ni,Zn)Ti_2O_5$ in AT2 and high-entropy $(Cr,Mn,Fe,Al,Ga)_2TiO_5$ in B2T are shown in Fig. 7. In AT2, the transition phase high-entropy $(Mg,Co,Ni,Zn)TiO_3$ phase is firstly generated through the solid-phase reaction between the raw material powders. Subsequently, high-entropy $(Mg,Co,Ni,Zn)TiO_3$ further reacts with TiO_2 to form high-entropy $(Mg,Co,Ni,Zn)Ti_2O_5$. Finally, a pure high-entropy pseudobrookite $(Mg,Co,Ni,Zn)Ti_2O_5$ is formed. In B2T, high-entropy spinel phase $(Cr,Mn,Fe,Al,Ga,Ti)_3O_4$ appears first, and eventually co-exists with high-entropy $(Cr,Mn,Fe,Al,Ga)_2TiO_5$. Finally, a biphasic

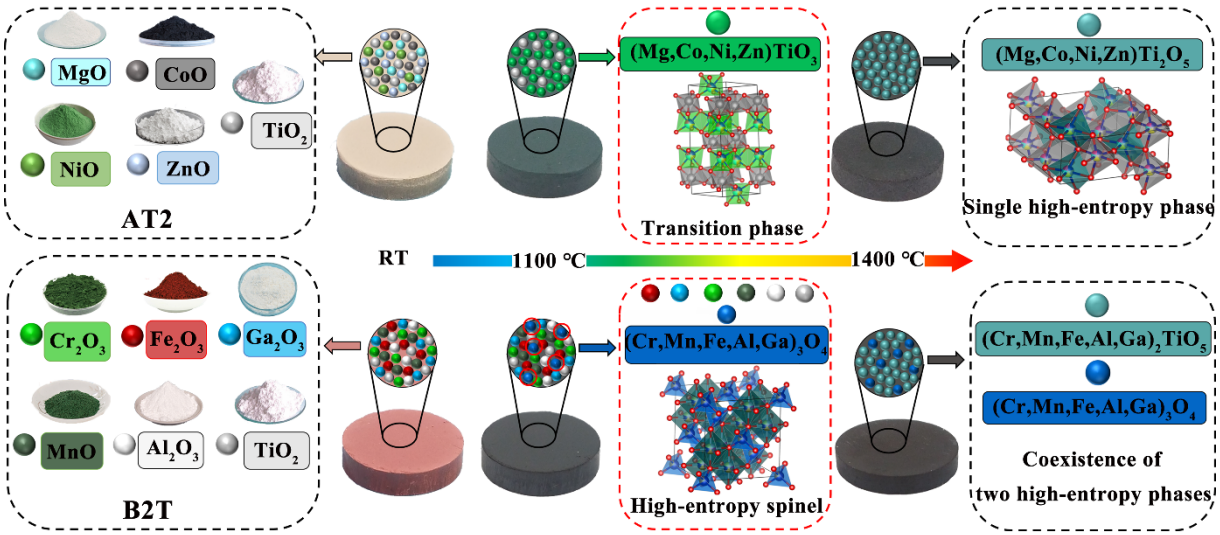

Fig. 7 Synthesis process of high-entropy $(Mg,Co,Ni,Zn)Ti_2O_5$ in AT2 and high-entropy $(Cr,Mn,Fe,Al,Ga)_2TiO_5$ in B2T.

high-entropy ceramic composed of the high-entropy pseudobrookite $(Cr,Mn,Fe,Al,Ga)_2TiO_5$ and the high-entropy spinel $(Cr,Mn,Fe,Al,Ga,Ti)_3O_4$ is formed.

Therefore, in order to investigate the crystal structure and the intrinsic property of the high-entropy pseudobrookite phase, the pure high-entropy $(Mg,Co,Ni,Zn)Ti_2O_5$ was selected as the research subject in Sections 3.3 and 3.4.

3. 3 Structure analysis of high-entropy pseudobrookite $(Mg,Co,Ni,Zn)Ti_2O_5$

The X-ray photoelectron spectroscopy (XPS) test can not only express the chemical states of elements, but also reflect the chemical environment of the metal elements. Figure 8 shows the XPS spectra of Mg 1s, Co 2p, Ni 2p, Zn 2p, and Ti 2p in high-entropy $(Mg,Co,Ni,Zn)Ti_2O_5$. For comparison, $MgTi_2O_5$, $CoTi_2O_5$, $NiTiO_3$, and $ZnTiO_3$ prepared by the same *in-situ* solid-phase reaction method were also analysed by the XPS in Fig. 8. It should be noted that since $NiTi_2O_5$ and $ZnTi_2O_5$ are unstable, $NiTiO_3$ and $ZnTiO_3$, which also have $[MO_6]$ octahedral, were chosen to analyse the chemical states and the chemical environment of the Zn and Ti elements.

For the pseudobrookite, both metal M and Ti ions should be in octahedral coordination. With regard to the Mg ions, the binding energies of Mg 1s in high-entropy $(Mg,Co,Ni,Zn)Ti_2O_5$ and $MgTi_2O_5$ are 1303.32 and 1303.16 eV, respectively, which are consistent with the binding energy of typical octahedrally coordinated Mg^{2+} [55]. The results denote that the Mg ions in high-entropy $(Mg,Co,Ni,Zn)Ti_2O_5$ belong to octahedrally coordinated Mg^{2+}. The peaks of the Co ions in high-entropy $(Mg,Co,Ni,Zn)Ti_2O_5$ situated at 796.42 and 780.63 eV can be accordingly assigned to Co $2p_{1/2}$ and Co $2p_{3/2}$, respectively, and the intense satellite peaks at 786.77 and 802.55 eV imply the presence of octahedrally coordinated Co^{2+} with high spin state [56]. The $CoTi_2O_5$ also shows almost the same binding energy and peak shape in Fig. 8. The results indicate that the Co ions in high-entropy $(Mg,Co,Ni,Zn)Ti_2O_5$ also belong to octahedrally coordinated Co^{2+}. As to the Ni ions in high-entropy $(Mg,Co,Ni,Zn)Ti_2O_5$, the binding energies of Ni $2p_{1/2}$ and $2p_{3/2}$ are 873.38 and 855.76 eV, respectively, which are consistent with the binding energy of the Ni^{2+} in typical Ni insulator [57,58]. Furthermore, the strong satellite peaks at 861.59 and 879.34 eV are similar with the satellite structure of high-spin Ni^{2+} in octahedral position [56]. In order to further confirm the chemical environment of the Ni in high-entropy $(Mg,Co,Ni,Zn)Ti_2O_5$, the XPS spectrum of Ni $2p_{3/2}$ and corresponding satellite peak of high-entropy $(Mg,Co,Ni,Zn)Ti_2O_5$ were fitted with five peaks. It is found that the peak shape of peak E is similar to that of $NiFe_2O_4$ with octahedral $[NiO_6]$ rather than that of $NiCr_2O_4$ with tetrahedral $[NiO_4]$ [59]. In addition, the $NiTiO_3$ with the same octahedrally coordinated Ni^{2+} has similar binding energy and peak shape. The results imply that the Ni ions in high-entropy $(Mg,Co,Ni,Zn)Ti_2O_5$ are octahedrally coordinated Ni^{2+}. For the Zn ions in high-entropy $(Mg,Co,Ni,Zn)Ti_2O_5$, the binding energies of Zn $2p_{3/2}$ and Zn $2p_{1/2}$ are 1021.30 and 1044.21 eV, respectively, which are consistent with the binding energy of typical Zn^{2+} [28,35].

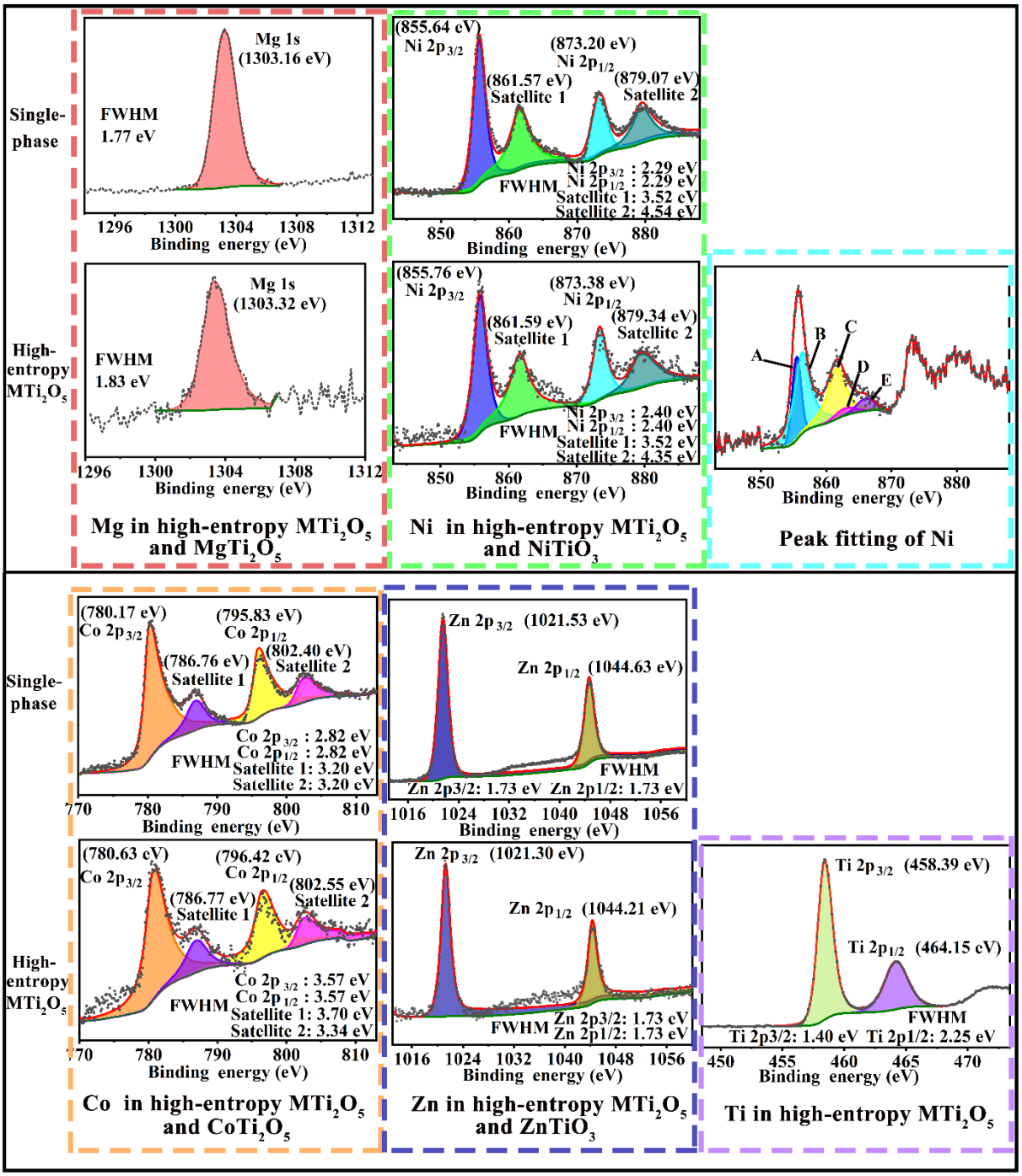

Fig. 8 High-resolution XPS spectra of Mg 1s, Co 2p, Ni 2p, Zn 2p, and Ti 2p in high-entropy $(Mg,Co,Ni,Zn)Ti_2O_5$ and corresponding normal pseudobrookite ceramics; and peak fitting of Ni $2p_{3/2}$ and satellite peak of high-entropy $(Mg,Co,Ni,Zn)Ti_2O_5$. FWHM represents the full width at half maximum.

The corresponding binding energies in $ZnTiO_3$ are 1021.53 and 1044.63 eV, which are similar to the binding energy of the Zn ions in high-entropy $(Mg,Co,Ni,Zn)Ti_2O_5$. The results suggest that the Zn ions in high-entropy $(Mg,Co,Ni,Zn)Ti_2O_5$ are also octahedrally coordinated Zn^{2+}. In conclusion, the XPS results indicate that the Mg, Co, Ni, and Zn ions in high-entropy $(Mg,Co,Ni,Zn)Ti_2O_5$ are all in octahedral coordination, which are consistent with the M ions in high-entropy pseudobrookite. Figure 8 also shows the XPS spectra of Ti 2p in high-entropy $(Mg,Co,Ni,Zn)Ti_2O_5$; the peaks situated at 458.39 and 464.15 eV belong to

Ti $2p_{3/2}$ and Ti $2p_{1/2}$, respectively, and demonstrate that the Ti ions in high-entropy $(Mg,Co,Ni,Zn)Ti_2O_5$ are Ti^{4+} rather than Ti^{3+}.

In order to analyze the configurational entropy change of high-entropy $(Mg,Co,Ni,Zn)Ti_2O_5$, the structural parameters were refined by using the Rietveld method and Fullprof software (Fig. 9). The refinement process was based on the crystal structure of $CoTi_2O_5$, and the change of configurational entropy can be reflected by the change of the cell parameters. Compared with the unit cell parameters of $CoTi_2O_5$ (a = 3.7320 Å, b = 9.7180 Å, and c = 10.0690 Å), the length of a and b in high-entropy $(Mg,Co,Ni,Zn)Ti_2O_5$ increases to 3.7415 and 9.7184 Å, respectively, while the length of c decreases to 10.0280 Å. The change of the cell parameters indicates an increase of configurational entropy of high-entropy $(Mg,Co,Ni,Zn)Ti_2O_5$ [20]. In addition, compared with the unit cell volume of $CoTi_2O_5$ (365.18 $Å^3$), the unit cell volume of high-entropy $(Mg,Co,Ni,Zn)Ti_2O_5$ is reduced to 364.63 $Å^3$, because the ion radius of Mg^{2+} (0.72 Å), Ni^{2+} (0.69 Å), and Zn^{2+} (0.74 Å) are all smaller than that of the Co^{2+} (0.75 Å) with high spin state.

Figure 10 shows the high-resolution TEM (HRTEM) image of high-entropy $(Mg,Co,Ni,Zn)Ti_2O_5$ and the selected area electron diffraction (SAED) pattern of the corresponding region. In the HRTEM image, three groups of crystal planes with interplanar spacings of 0.2109, 0.2315, and 0.1943 nm are assigned to the (024), (130), and (114) crystal planes in the pseudobrookite structure, respectively. The periodic lattice structure in the HRTEM image and the corresponding SAED pattern along the $[6\bar{2}\bar{1}]$ direction confirm that the crystal structure of synthesized high-entropy $(Mg,Co,Ni,Zn)Ti_2O_5$ belongs to the pseudobrookite structure.

Figures 11(a) and 11(b) show the atomic-resolution STEM–high-angle annular dark-field (HAADF) images of high-entropy $(Mg,Co,Ni,Zn)Ti_2O_5$. It can be seen that high-entropy $(Mg,Co,Ni,Zn)Ti_2O_5$ is orderly

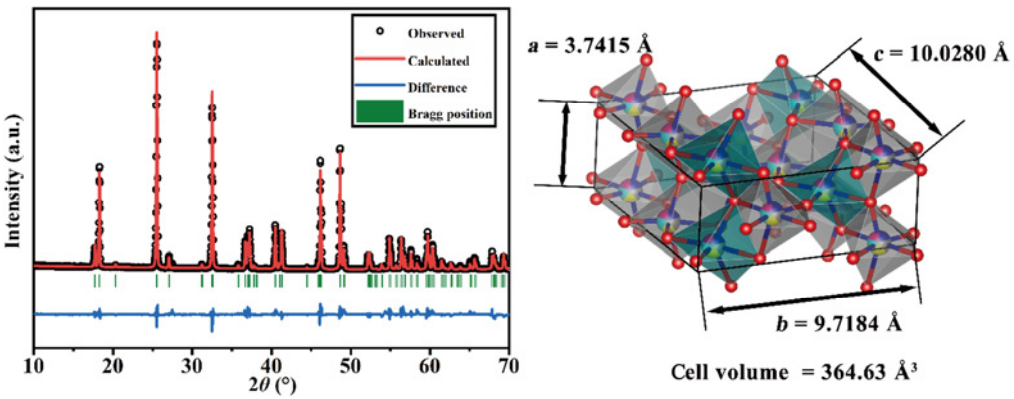

Fig. 9 Rietveld analysis of the XRD patterns.

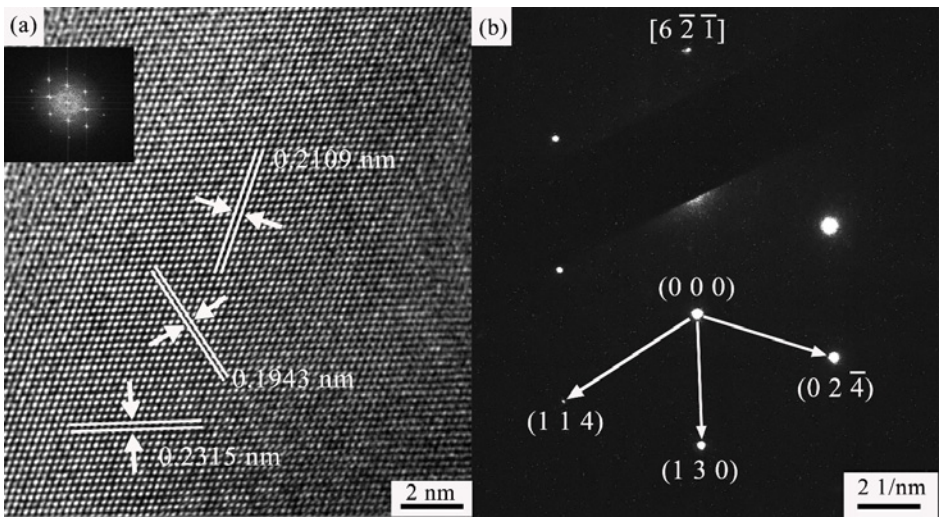

Fig. 10 (a) HRTEM image of high-entropy $(Mg,Co,Ni,Zn)Ti_2O_5$ and (b) corresponding SAED pattern.

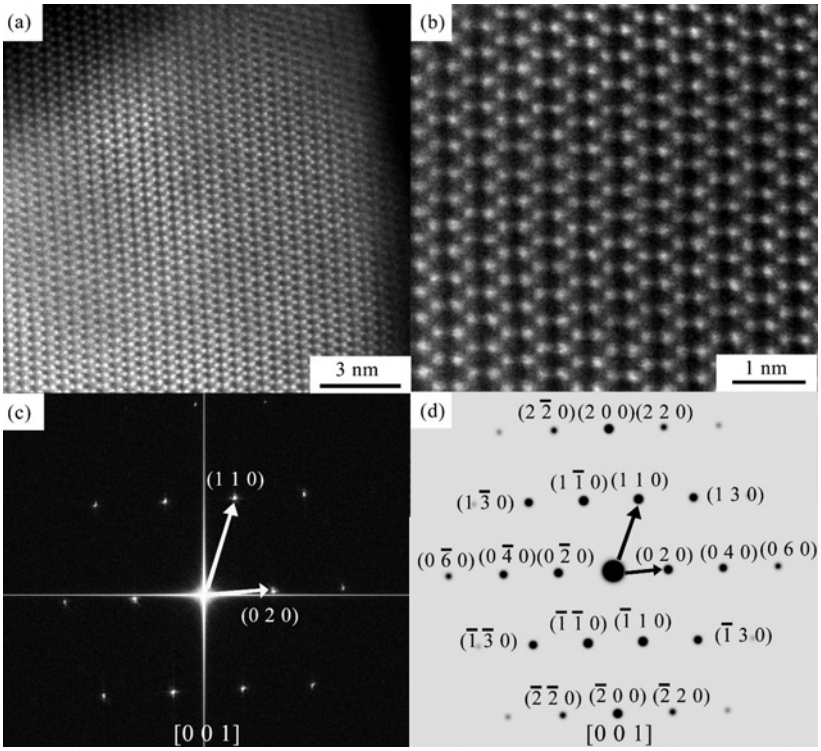

Fig. 11 Atomic-resolution STEM–HAADF images of high-entropy $(Mg,Co,Ni,Zn)Ti_2O_5$ at (a) low and (b) high magnifications; (c) corresponding SAED pattern; and (d) simulated pattern of the standard pseudobrookite phase taken from the [001] direction.

arranged on the atomic scale. Figure 11(c) shows the corresponding SAED pattern; Fig. 11(d) shows the simulated pattern of the standard pseudobrookite phase taken from the [001] direction, which was constructed from the crystallographic information file (CIF) of the pseudobrookite phase. By comparing Fig. 11(c) and Fig. 11(d), the SAED pattern (Fig. 11(c)) is exactly the same as the simulated pattern (Fig. 11(a)), indicating that the STEM image (Fig. 11(b)) is the (001) crystal plane in the pseudobrookite structure.

Figure 12(a) shows the theoretical crystal structure of pseudobrookite with the viewing direction perpendicular to the *ab* plane. The red, green, and gray spheres represent the O ions, the metal M ions occupying the A site, and the Ti ions occupying the B site in the pseudobrookite structure, respectively. Figure 12(b) shows the simplified crystal structure of Fig. 12(a) after the removal of O ions. It can be seen that the metal M ions in A site and the Ti ions in B site are arranged in a serpentine double chain-like structure along the *a*-axis direction. This serpentine double chain-like structure contains two types of "nodes" with different distances, which are framed by blue and red rectangles. As shown in the HAADF image in the same viewing direction (Fig. 12(c)), the metal M and Ti ions in high-entropy $(Mg,Co,Ni,Zn)Ti_2O_5$ exhibit the similar serpentine chain-like structure. However, the theoretical crystal structure of pseudobrookite and the actual crystal structure of high-entropy $(Mg,Co,Ni,Zn)Ti_2O_5$ show different "nodes" in the chain-like structure.

Figure 12(d) shows the theoretical crystal structure of pseudobrookite viewed from the direction perpendicular to the *a* axis. It is clearly seen that the metal M ions at the A site and the Ti ions at the B site do not overlap each other completely in each "node" of the chain-like structure, resulting in a "diatomic" state of each "node" in the direction perpendicular to the *c* axis (Fig. 12(b)). In contrast, the chain-like structure of high-entropy $(Mg,Co,Ni,Zn)Ti_2O_5$ shows a "single atom" state at each "node" (Fig. 12(c)). This "single atom" state in the (001) crystal plane of high-entropy $(Mg,Co,Ni,Zn)Ti_2O_5$ is consistent with that of the ideal crystal structure of the high-entropy pseudobrookite phase (Fig. 1(b)), and indicates that the metal M and Ti ions are randomly distributed at the A site and the B site.

Figures 12(e) and 12(f) show the single unit cell of the theoretical pseudobrookite crystal structure and the HAADF image at high magnification of high-entropy $(Mg,Co,Ni,Zn)Ti_2O_5$ (the image contrast was improved

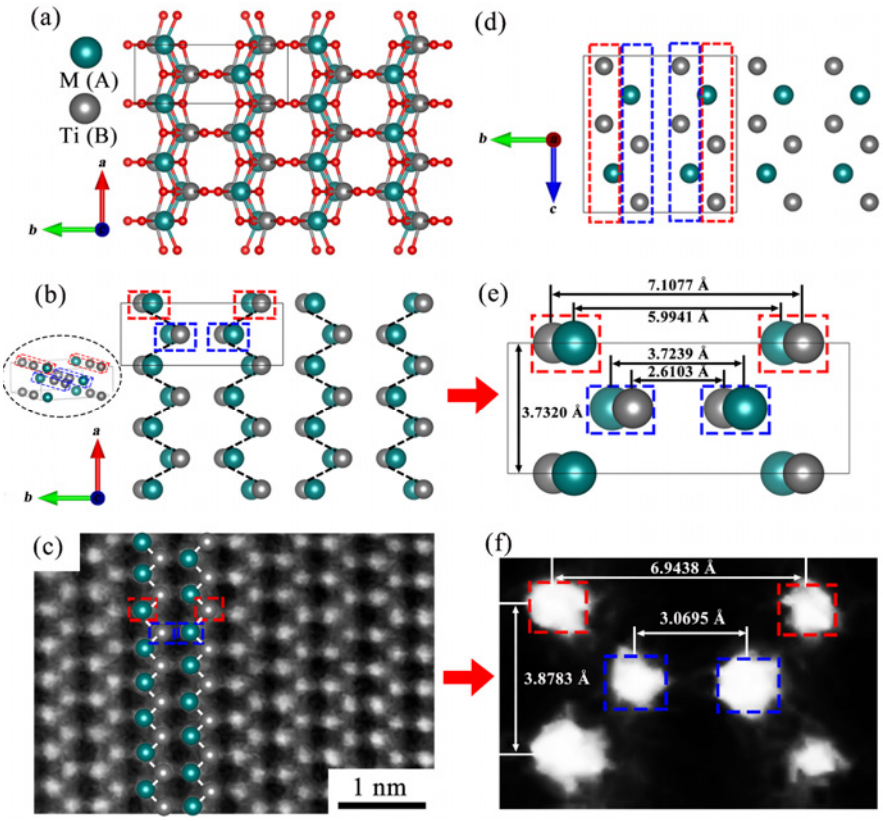

Fig. 12 (a, b, d) Theoretical crystal structures of the pseudobrookite phase. (c) HAADF image of high-entropy (Mg,Co,Ni,Zn)Ti_2O_5. (e) Single unit cell of theoretical crystal structure. (f) HAADF image at high magnification of high-entropy (Mg,Co,Ni,Zn)Ti_2O_5 taken from the same direction.

by the photoshop software), respectively. In the theoretical crystal structure of pseudobrookite (Fig. 12(e)), the distances between M at the A site and Ti at the B site in the two blue "nodes" are 3.7239 and 2.6103 Å, respectively. In high-entropy (Mg,Co,Ni,Zn)Ti_2O_5 (Fig. 12(f)), the distance between these ions in the two blue "nodes" is 3.0695 Å, which is between 2.6103 and 3.7239 Å. Similarly, the distances between M at the A site and Ti at the B site in the red "node" are 5.9941 and 7.1077 Å in the theoretical crystal structure of pseudobrookite, and that in high-entropy (Mg,Co,Ni,Zn)Ti_2O_5 is 6.9438 Å, between 5.9941 and 7.1077 Å. This phenomenon further exhibits the random assignment of metal M and Ti ions at the A and the B site in high-entropy (Mg,Co,Ni,Zn)Ti_2O_5. Furthermore, it is worth noting that the cell parameters of the *a* and *b* axes obtained in the HAADF image at high magnetism (Fig. 12(f)) are 3.8783 and 10.0133 Å, respectively, which are much higher than those of any known pseudobrookite titanate ceramic, indicating that high-entropy (Mg,Co,Ni,Zn)Ti_2O_5 has an unprecedented high configurational entropy [20].

3.4 Properties of high-entropy pseudobrookite (Mg,Co,Ni,Zn)Ti_2O_5

The biggest disadvantage of pseudobrookite is that it is easy to decomposing below 1200 ℃. For instance, the $MgTi_2O_5$ phase decomposed at 130–230 or below 620 ℃ [23,42], the $CoTi_2O_5$ phase was unstable below 1200 ℃ [45], and the $ZnTi_2O_5$ phase decomposed when heated in the air [35]. Therefore, in order to explore the thermal stability of high-entropy (Mg,Co,Ni,Zn)Ti_2O_5, the sample was heated at 200, 600, and 1400 ℃ for 20 h. Figure 13(a) shows the XRD results of the samples after heated at different temperatures. Unlike normal pseudobrookite, high-entropy (Mg,Co,Ni,Zn)Ti_2O_5 does not decompose after heated at different temperatures, and no other phases are formed. High-entropy (Mg,Co,Ni,Zn)Ti_2O_5 has higher configurational entropy and lower Gibbs free energy than the normal pseudobrookite titanate ceramics, and thus exhibits an excellent stability. However, it can be seen that the relative intensity of some peaks in the XRD spectrum of high-entropy (Mg,Co,Ni,Zn)Ti_2O_5 change after the heat treatment at

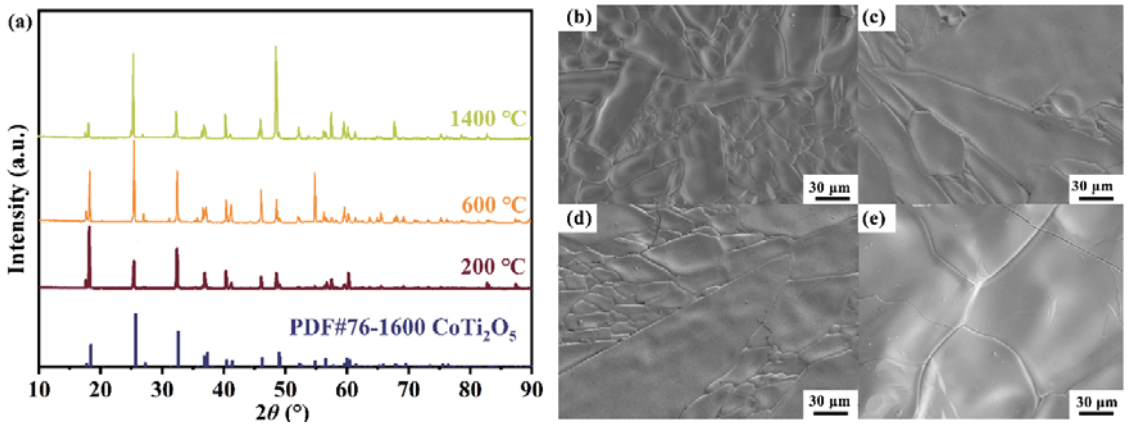

Fig. 13 (a) XRD patterns of high-entropy $(Mg,Co,Ni,Zn)Ti_2O_5$ after heat treatment at 200, 600, and 1400 ℃ for 20 h. SEM images of high-entropy $(Mg,Co,Ni,Zn)Ti_2O_5$ (b) before heat treatment and after heat treatment at (c) 200 ℃, (d) 600 ℃, and (e) 1400 ℃.

different temperatures, which is attributed to a combination of the continuous growth of some crystal planes at high temperatures and the oriented arrangement of rod-shaped particles under pressure [60–64]. Figures 13(b)–13(d) show the SEM images of the surface morphology of high-entropy $(Mg,Co,Ni,Zn)Ti_2O_5$ before heat treatment and after heat treatment at different temperatures. It is demonstrated that continuous growth of crystal planes occurred to different degrees of high-entropy $(Mg,Co,Ni,Zn)Ti_2O_5$ after heat treatment at different temperatures, which led to the changes in relative intensity of some peaks in the XRD spectra.

Figure 14(a) shows the thermal expansion curve and the corresponding thermal expansion coefficients of high-

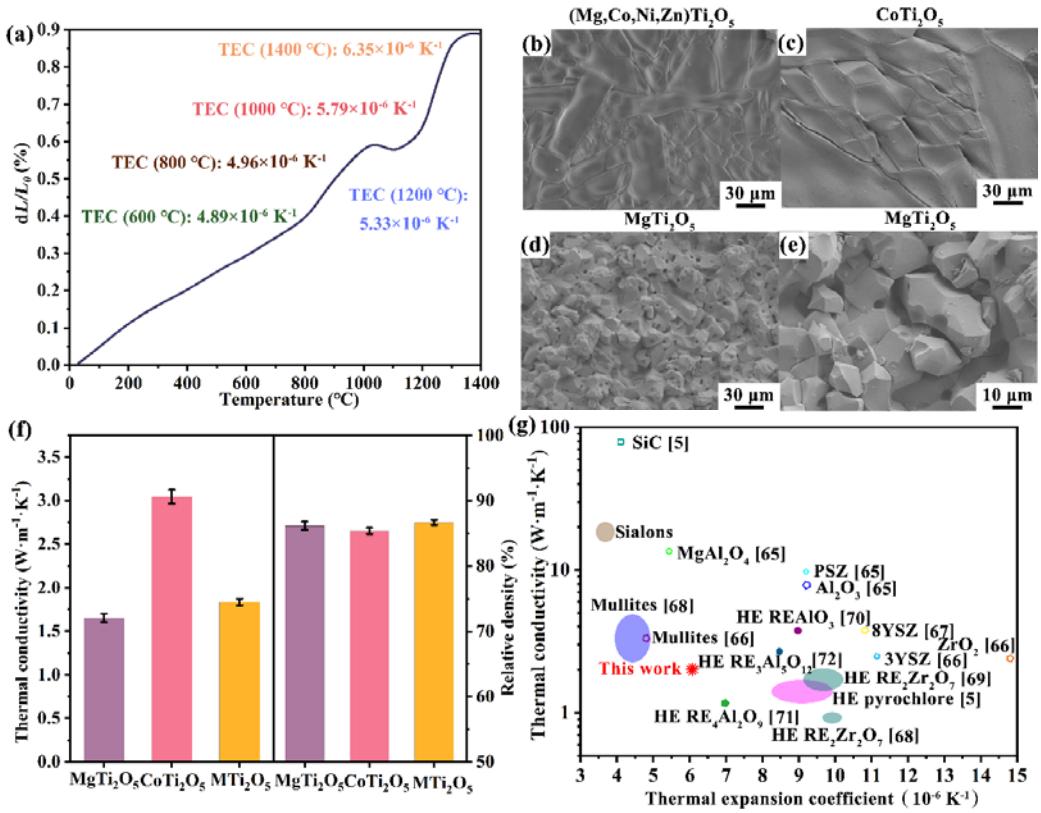

Fig. 14 (a) Thermal expansion curve and thermal expansion coefficients of high-entropy $(Mg,Co,Ni,Zn)Ti_2O_5$. (b–e) SEM images and (f) relative densities and thermal conductivities of high-entropy $(Mg,Co,Ni,Zn)Ti_2O_5$, $CoTi_2O_5$, and $MgTi_2O_5$. (g) Thermal conductivity vs. thermal expansion coefficient.

entropy (Mg,Co,Ni,Zn)Ti_2O_5. The thermal expansion coefficient of high-entropy (Mg,Co,Ni,Zn)Ti_2O_5 in the range of 25–1400 ℃ is 6.35×10^{-6} K^{-1}. The decrease of thermal expansion coefficient in the range of 1000–1200 ℃ is attributed to the healing of microcracks in the pseudobrookite phase at high temperatures [24,31].

Figures 14(b)–14(f) show the morphology images and the relative densities and the thermal conductivities at RT of high-entropy (Mg,Co,Ni,Zn)Ti_2O_5, $CoTi_2O_5$, and $MgTi_2O_5$ prepared by the same method. The thermal conductivity of ceramic depends mainly on the crystal structure, the grain size, and the number and size of pores. High-entropy (Mg,Co,Ni,Zn)Ti_2O_5, $CoTi_2O_5$, and $MgTi_2O_5$ have almost the same relative densities. Moreover, high-entropy (Mg,Co,Ni,Zn)Ti_2O_5 and $CoTi_2O_5$ also have similar morphologies and grain sizes. However, the thermal conductivity of high-entropy (Mg,Co,Ni,Zn)Ti_2O_5 (1.840 $W\cdot m^{-1}\cdot K^{-1}$) is much smaller than that of $CoTi_2O_5$ (3.045 $W\cdot m^{-1}\cdot K^{-1}$). Severe lattice distortion and the synergistic effect of multi-component cations reduce the thermal conductivity of high-entropy (Mg,Co,Ni,Zn)Ti_2O_5. For $MgTi_2O_5$ with similar relative density, the smaller particle size and the large number of fine pores reduce the apparent thermal conductivity of $MgTi_2O_5$, resulting in a slightly lower thermal conductivity (1.642 $W\cdot m^{-1}\cdot K^{-1}$) of $MgTi_2O_5$ than that of high-entropy (Mg,Co,Ni,Zn)Ti_2O_5 (1.840 $W\cdot m^{-1}\cdot K^{-1}$).

Figure 14(g) summarized the thermal conductivity vs. thermal expansion coefficient for high-entropy (Mg,Co,Ni,Zn)Ti_2O_5 with commonly used thermal insulation materials and some reported high-entropy ceramics. Compared with conventional thermal resistant insulation ceramics [5,65–68] and some reported high-entropy ceramics [68–74], high-entropy (Mg,Co,Ni,Zn)Ti_2O_5 exhibits both low thermal expansion coefficient and low thermal conductivity. The lower thermal expansion coefficient can reduce the thermal stress of the thermal insulation materials, while the lower thermal conductivity can effectively insulate the heat [22,75]. Therefore, high-entropy (Mg,Co,Ni,Zn)Ti_2O_5 has a great potential for the thermal protection systems.

4 Conclusions

In this work, high-entropy pseudobrookite is successfully synthesized for the first time. The pure high-entropy pseudobrookite (Mg,Co,Ni,Zn)Ti_2O_5, the biphasic high-entropy ceramic composed of the high-entropy pseudobrookite $(Cr,Mn,Fe,Al,Ga)_2TiO_5$ and the high-entropy spinel $(Cr,Mn,Fe,Al,Ga,Ti)_3O_4$ are prepared by the solid-phase reaction method. The crystal structure and properties of high-entropy (Mg,Co,Ni,Zn)Ti_2O_5 are studied in depth. By comparing the AC-STEM images of high-entropy (Mg,Co,Ni,Zn)Ti_2O_5 with the theoretical crystal structure of normal pseudobrookite ceramic, we find that high-entropy (Mg,Co,Ni,Zn)Ti_2O_5 not only exhibits the same disordered distribution between metal M ions at the A site as the normal high-entropy ceramics, but also the disorder of the distribution of metal M and Ti ions between the A site and the B site is also greatly increased compared to that of the normal pseudobrookite ceramic. The cell parameters further indicate that high-entropy (Mg,Co,Ni,Zn)Ti_2O_5 has an unprecedented high configurational entropy. At the same time, the dense high-entropy (Mg,Co,Ni,Zn)Ti_2O_5 shows a low thermal expansion coefficient of 6.35×10^{-6} K^{-1} in the temperature range of 25–1400 ℃ and a low thermal conductivity of 1.840 $W\cdot m^{-1}\cdot K^{-1}$ at RT, as well as an excellent thermal stability at different temperatures. These outstanding properties make high-entropy (Mg,Co,Ni,Zn)Ti_2O_5 have a great potential for the application in thermal protection systems.

Acknowledgements

The authors acknowledge the financial support from the National Natural Science Foundation of China (No. 52172072).

Declaration of competing interest

The authors have no competing interests to declare that are relevant to the content of this article.

References

[1] Cantor B, Chang ITH, Knight P, *et al*. Microstructural development in equiatomic multicomponent alloys. *Mater Sci Eng A* 2004, **375–377**: 213–218.

[2] Yeh JW, Chen SK, Lin SJ, *et al*. Nanostructured high-entropy alloys with multiple principal elements: Novel alloy design concepts and outcomes. *Adv Eng Mater* 2004, **6**: 299–303.

[3] Rost CM, Sachet E, Borman T, *et al*. Entropy-stabilized oxides. *Nat Commun* 2015, **6**: 8485.

[4] Oses C, Toher C, Curtarolo S. High-entropy ceramics. *Nat Rev Mater* 2020, **5**: 295–309.

[5] Xiang HM, Xing Y, Dai FZ, *et al*. High-entropy ceramics: Present status, challenges, and a look forward. *J Adv Ceram* 2021, **10**: 385–441.

[6] Zhang WM, Zhao B, Xiang HM, *et al*. One-step synthesis and electromagnetic absorption properties of high entropy rare earth hexaborides (HE REB_6) and high entropy rare earth hexaborides/borates (HE REB_6/HE $REBO_3$) composite powders. *J Adv Ceram* 2021, **10**: 62–77.

[7] Li F, Zhou L, Liu JX, *et al*. High-entropy pyrochlores with low thermal conductivity for thermal barrier coating materials. *J Adv Ceram* 2019, **8**: 576–582.

[8] Jiang SC, Hu T, Gild J, *et al*. A new class of high-entropy perovskite oxides. *Scripta Mater* 2018, **142**: 116–120.

[9] Liu SY, Zhang SX, Liu SY, *et al*. Stability and mechanical properties of single-phase quinary high-entropy metal carbides: First-principles theory and thermodynamics. *J Eur Ceram Soc* 2022, **42**: 3089–3098.

[10] Strauss F, Lin J, Duffiet M, *et al*. High-entropy polyanionic lithium superionic conductors. *ACS Mater Lett* 2022, **4**: 418–423.

[11] Xue Y, Zhao XQ, An YL, *et al*. High-entropy $(La_{0.2}Nd_{0.2}Sm_{0.2}Eu_{0.2}Gd_{0.2})_2Ce_2O_7$: A potential thermal barrier material with improved thermo-physical properties. *J Adv Ceram* 2022, **11**: 615–628.

[12] Wright AJ, Luo J. A step forward from high-entropy ceramics to compositionally complex ceramics: A new perspective. *J Mater Sci* 2020, **55**: 9812–9827.

[13] Qin MD, Vega H, Zhang DW, *et al*. 21-Component compositionally complex ceramics: Discovery of ultrahigh-entropy weberite and fergusonite phases and a pyrochlore–weberite transition. *J Adv Ceram* 2022, **11**: 641–655.

[14] Qin Y, Liu JX, Li F, *et al*. A high entropy silicide by reactive spark plasma sintering. *J Adv Ceram* 2019, **8**: 148–152.

[15] Gild J, Braun J, Kaufmann K, *et al*. A high-entropy silicide: $(Mo_{0.2}Nb_{0.2}Ta_{0.2}Ti_{0.2}W_{0.2})Si_2$. *J Materiomics* 2019, **5**: 337–343.

[16] Liu JX, Shen XQ, Wu Y, *et al*. Mechanical properties of hot-pressed high-entropy diboride-based ceramics. *J Adv Ceram* 2020, **9**: 503–510.

[17] Gild J, Zhang YY, Harrington T, *et al*. High-entropy metal diborides: A new class of high-entropy materials and a new type of ultrahigh temperature ceramics. *Sci Rep* 2016, **6**: 37946.

[18] Chen H, Xiang HM, Dai FZ, *et al*. Porous high entropy $(Zr_{0.2}Hf_{0.2}Ti_{0.2}Nb_{0.2}Ta_{0.2})B_2$: A novel strategy towards making ultrahigh temperature ceramics thermal insulating. *J Mater Sci Technol* 2019, **35**: 2404–2408.

[19] Xirouchakis DM. Pseudobrookite-group oxide solutions and basaltic melts. *Lithos* 2007, **95**: 1–9.

[20] Yang HX, Hazen RM. Crystal chemistry of cation order–disorder in pseudobrookite-type $MgTi_2O_5$. *J Solid State Chem* 1998, **138**: 238–244.

[21] Xirouchakis D, Smirnov A, Woody K, *et al*. Thermodynamics and stability of pseudobrookite-type $MgTi_2O_5$ (karrooite). *Am Mineral* 2002, **87**: 658–667.

[22] Wu JY, Xu XJ, Xiong YL, *et al*. Preparation and structure control of a scalelike $MoSi_2$–borosilicate glass coating with improved contact damage and thermal shock resistance. *Ceram Int* 2020, **46**: 7178–7186.

[23] Suzuki Y, Shinoda Y. Magnesium dititanate ($MgTi_2O_5$) with pseudobrookite structure: A review. *Sci Technol Adv Mater* 2011, **12**: 034301.

[24] Kornaus K, Rutkowski P, Lach R, *et al*. Effect of microstructure on thermal and mechanical properties of solid solutions Al_2TiO_5–$MgTi_2O_5$. *J Eur Ceram Soc* 2021, **41**: 1498–1505.

[25] Nakagoshi Y, Suzuki Y. Pseudobrookite-type $MgTi_2O_5$ water purification filter with controlled particle morphology. *J Asian Ceram Soc* 2015, **3**: 334–338.

[26] Regue M, Ahmet IY, Bassi PS, *et al*. Zn-doped Fe_2TiO_5 pseudobrookite-based photoanodes grown by aerosol-assisted chemical vapor deposition. *ACS Appl Energ Mater* 2020, **3**: 12066–12077.

[27] Platt NJ, Kaye KM, Limburn GJ, *et al*. Order of magnitude increase in photocatalytic rate for hierarchically porous anatase thin films synthesized from zinc titanate coatings. *Dalton Trans* 2017, **46**: 1975–1985.

[28] Xiong K, Wang KZ, Chen L, *et al*. Heterostructured $ZnFe_2O_4$/Fe_2TiO_5/TiO_2 composite nanotube arrays with an improved photocatalysis degradation efficiency under simulated sunlight irradiation. *Nano-Micro Lett* 2018, **10**: 17.

[29] Ehsan MA, Naeem R, McKee V, *et al*. $MgTi_2O_5$ thin films from single molecular precursor for photoelectrochemical water splitting. *Sol Energ Mat Sol C* 2017, **161**: 328–337.

[30] Zhang N, Zhang KF, Zhou W, *et al*. Pure phase orthorhombic $MgTi_2O_5$ photocatalyst for H_2 production. *RSC Adv* 2015, **5**: 106151–106155.

[31] Chen C, Giovannelli F, Duclère JR, *et al*. Thermoelectric properties of $Fe_2(Ti_{1-x}Nb_x)O_5$ pseudobrookite ceramics with low thermal conductivity. *J Eur Ceram Soc* 2017, **37**: 4681–4685.

[32] Djuric ZZ, Aleksic OS, Nikolic MV, *et al*. Structural and electrical properties of sintered Fe_2O_3/TiO_2 nanopowder mixtures. *Ceram Int* 2014, **40**: 15131–15141.

[33] Nikolic MV, Vasiljevic ZZ, Lukovic MD, *et al*. Humidity sensing properties of nanocrystalline pseudobrookite (Fe_2TiO_5) based thick films. *Sensor Actuat B-Chem* 2018, **277**: 654–664.

[34] Sarwanto Y, Adi WA. Modification of pseudobrookite $Fe_{2-x}Mn_xTiO_5$ with solid state reaction method using a mechanical milling. *IOP Conf Ser Mater Sci Eng* 2017, **202**: 012073.

[35] Perry NH, Stevanovic V, Lim LY, *et al*. Discovery of a ternary pseudobrookite phase in the earth-abundant Ti–Zn–O system. *Dalton Trans* 2016, **45**: 1572–1581.

[36] Cerro S, Gargori C, Llusar M, *et al*. Orthorhombic (Fe_2TiO_5)–monoclinic (Cr_2TiO_5) solid solution series: Synthesis by gel routes, coloring and NIR reflectivity evaluation. *Ceram Int* 2018, **44**: 13349–13359.

[37] Llusar M, García E, García MT, *et al*. Synthesis, stability and coloring properties of yellow–orange pigments based on Ni-doped karrooite (Ni,Mg)Ti_2O_5. *J Eur Ceram Soc* 2015, **35**: 357–376.

[38] Llusar M, Bermejo T, Primo JE, *et al*. Karrooite green pigments doped with Co and Zn: Synthesis, color properties and stability in ceramic glazes. *Ceram Int* 2017, **43**: 9133–9144.

[39] Matteucci F, Cruciani G, Dondi M, *et al*. Crystal structure, optical properties and colouring performance of karrooite $MgTi_2O_5$ ceramic pigments. *J Solid State Chem* 2007, **180**: 3196–3210.

[40] Dondi M, Lyubenova TS, Carda JB, *et al*. M-doped Al_2TiO_5 (M = Cr, Mn, Co) solid solutions and their use as ceramic pigments. *J Am Ceram Soc* 2009, **92**: 1972–1980.

[41] Kornaus K, Lach R, Szumera M, *et al*. Synthesis of aluminium titanate by means of isostructural heterogeneous nucleation. *J Eur Ceram Soc* 2019, **39**: 2535–2544.

[42] Jantzen T, Hack K, Yazhenskikh E, *et al*. Addition of TiO_2 and Ti_2O_3 to the Al_2O_3–FeO–Fe_2O_3–MgO system. *Calphad* 2018, **62**: 187–200.

[43] Jaromin AL, Edwards DD. Subsolidus phase relationships in the Ga_2O_3–Al_2O_3–TiO_2 system. *J Am Ceram Soc* 2005, **88**: 2573–2577.

[44] Korim T. Effect of Mg^{2+}- and Fe^{3+}-ions on formation mechanism of aluminium titanate. *Ceram Int* 2009, **35**: 1671–1675.

[45] Anderson KP, Giri AK, Vinci RP, *et al*. Single crystal growth of $CoTi_2O_5$ by solid state reaction synthesis. *J Am Ceram Soc* 2019, **102**: 5050–5062.

[46] Deng YF, Zhang HL, Hong QM, *et al*. Titanium-based mixed oxides from a series of titanium(IV) citrate complexes. *J Solid State Chem* 2007, **180**: 3152–3159.

[47] Liou YC, Yang SL. Calcium-doped $MgTiO_3$–$MgTi_2O_5$ ceramics prepared using a reaction-sintering process. *Mater Sci Eng B* 2007, **142**: 116–120.

[48] Giordano L, Viviani M, Bottino C, *et al*. Microstructure and thermal expansion of Al_2TiO_5–$MgTi_2O_5$ solid solutions obtained by reaction sintering. *J Eur Ceram Soc* 2002, **22**: 1811–1822.

[49] Minouei H, Kheradmandfard M, Rizi MS, *et al*. Formation mechanism of high-entropy spinel thin film and its mechanical and magnetic properties: Linking high-entropy alloy to high-entropy ceramic. *Appl Surf Sci* 2022, **576**: 151719.

[50] Stygar M, Dąbrowa J, Moździerz M, *et al*. Formation and properties of high entropy oxides in Co–Cr–Fe–Mg–Mn–Ni–O system: Novel $(Cr,Fe,Mg,Mn,Ni)_3O_4$ and $(Co,Cr,Fe,Mg,Mn)_3O_4$ high entropy spinels. *J Eur Ceram Soc* 2020, **40**: 1644–1650.

[51] Parida T, Karati A, Guruvidyathri K, *et al*. Novel rare-earth and transition metal-based entropy stabilized oxides with spinel structure. *Scripta Mater* 2020, **178**: 513–517.

[52] Marik S, Singh D, Gonano B, *et al*. Enhanced magnetic frustration in a new high entropy diamond lattice spinel oxide. *Scripta Mater* 2020, **186**: 366–369.

[53] Fracchia M, Manzoli M, Anselmi-Tamburini U, *et al*. A new eight-cation inverse high entropy spinel with large configurational entropy in both tetrahedral and octahedral sites: Synthesis and cation distribution by X-ray absorption spectroscopy. *Scripta Mater* 2020, **188**: 26–31.

[54] Lin CC, Chang CW, Kaun CC, *et al*. Stepwise evolution of photocatalytic spinel-structured $(Co,Cr,Fe,Mn,Ni)_3O_4$ high entropy oxides from first-principles calculations to machine learning. *Crystals* 2021, **11**: 1035.

[55] Mittal VK, Chandramohan P, Bera S, *et al*. Cation distribution in $Ni_xMg_{1-x}Fe_2O_4$ studied by XPS and Mössbauer spectroscopy. *Solid State Commun* 2006, **137**: 6–10.

[56] Kim JG, Pugmire DL, Battaglia D, *et al*. Analysis of the $NiCo_2O_4$ spinel surface with Auger and X-ray photoelectron spectroscopy. *Appl Surf Sci* 2000, **165**: 70–84.

[57] Nesbitt HW, Legrand D, Bancroft GM. Interpretation of Ni2p XPS spectra of Ni conductors and Ni insulators. *Phys Chem Miner* 2000, **27**: 357–366.

[58] Sakamoto K, Hayashi F, Sato K, *et al*. XPS spectral analysis for a multiple oxide comprising NiO, TiO_2, and $NiTiO_3$. *Appl Surf Sci* 2020, **526**: 146729.

[59] Biesinger MC, Payne BP, Grosvenor AP, *et al*. Resolving surface chemical states in XPS analysis of first row transition metals, oxides and hydroxides: Cr, Mn, Fe, Co and Ni. *Appl Surf Sci* 2011, **257**: 2717–2730.

[60] Tang K, Wang CA, Xu XL, *et al*. A study on powder X-ray diffraction of Ti_3SiC_2. *Mater Lett* 2002, **55**: 50–54.

[61] Shi WT, Sun DL, Chen JQ, *et al*. Hydrothermal synthesis of aluminum-doped zincophosphate large single crystal with different morphology. *J Cryst Growth* 2019, **507**: 189–195.

[62] Inoue M, Hirasawa I. The relationship between crystal morphology and XRD peak intensity on $CaSO_4{\cdot}2H_2O$. *J Cryst Growth* 2013, **380**: 169–175.

[63] Matos CRS, Xavier MJ, Barreto LS, *et al*. Principal component analysis of X-ray diffraction patterns to yield morphological classification of brucite particles. *Anal Chem* 2007, **79**: 2091–2095.

[64] Heidarpour A, Aghamohammadi H, Jamshidi R, *et al*. The shape evolution of TiC_x prepared by mechanical alloying of Ti–Al–C system after HF treatment. *Ceram Int* 2019, **45**: 4653–4660.

[65] Sun ZQ, Zhou YC, Wang JY, *et al*. Thermal properties and thermal shock resistance of γ-$Y_2Si_2O_7$. *J Am Ceram Soc* 2008, **91**: 2623–2629.

[66] Cao XQ, Vassen R, Stoever D. Ceramic materials for thermal barrier coatings. *J Eur Ceram Soc* 2004, **24**: 1–10.

[67] Zhao M, Ren XR, Yang J, *et al*. Thermo-mechanical properties of ThO_2-doped Y_2O_3 stabilized ZrO_2 for thermal barrier coatings. *Ceram Int* 2016, **42**: 501–508.

[68] Zhao ZF, Xiang HM, Dai FZ, *et al*. $(La_{0.2}Ce_{0.2}Nd_{0.2}Sm_{0.2}Eu_{0.2})_2Zr_2O_7$: A novel high-entropy ceramic with low thermal conductivity and sluggish grain growth rate. *J Mater Sci Technol* 2019, **35**: 2647–2651.

[69] Zhu JT, Meng XY, Zhang P, *et al*. Dual-phase rare- earth-zirconate high-entropy ceramics with glass-like thermal

conductivity. *J Eur Ceram Soc* 2021, **41**: 2861–2869.

[70] Zhao ZF, Chen H, Xiang HM, *et al*. High-entropy $(Y_{0.2}Nd_{0.2}Sm_{0.2}Eu_{0.2}Er_{0.2})AlO_3$: A promising thermal/environmental barrier material for oxide/oxide composites. *J Mater Sci Technol* 2020, **47**: 45–51.

[71] Zhao ZF, Xiang HM, Chen H, *et al*. High-entropy $(Nd_{0.2}Sm_{0.2}Eu_{0.2}Y_{0.2}Yb_{0.2})_4Al_2O_9$ with good high temperature stability, low thermal conductivity, and anisotropic thermal expansivity. *J Adv Ceram* 2020, **9**: 595–605.

[72] Chen H, Zhao ZF, Xiang HM, *et al*. High entropy $(Y_{0.2}Yb_{0.2}Lu_{0.2}Eu_{0.2}Er_{0.2})_3Al_5O_{12}$: A novel high temperature stable thermal barrier material. *J Mater Sci Technol* 2020, **48**: 57–62.

[73] Qin MD, Yan QZ, Liu Y, *et al*. A new class of high-entropy M_3B_4 borides. *J Adv Ceram* 2021, **10**: 166–172.

[74] Zhang Y, Sun SK, Guo WM, *et al*. Optimal preparation of high-entropy boride–silicon carbide ceramics. *J Adv Ceram* 2021, **10**: 173–180.

[75] Wang MC, Bu FX, Zhou CJ, *et al*. Bonding performance and mechanism of a heat-resistant composite precursor adhesive (RT–1000 ℃) for TC4 titanium alloy. *J Micromech Mol Phys* 2020, **5**: 2050016.